Supporting Information

Going Beyond the Equilibrium Crystal Shape: Re-tracing the Morphological Evolution in Group 5 Tetradymite Nanocrystals

Woohyun Hwang,[1,*] Su-Hyun Yoo,[2,*] Aloysius Soon,[1,3,†] and Woosun Jang[1,4,‡]

[1]*Department of Materials Science & Engineering and*
Center for Artificial Synesthesia Materials Discovery,
Yonsei University, Seoul 03722, Republic of Korea
[2]*Department of Computational Materials Design,*
Max-Planck-Institut für Eisenforschung GmbH,
Max-Planck-Straße 1, 40237, Düsseldorf, Germany
[3]*School of Physics, The University of Sydney,*
New South Wales 2006, Sydney, Australia
[4]*Current address: Department of Inorganic Chemistry,*
Fritz-Haber-Institut der Max-Planck-Gesellschaft,
Faradayweg 4-6, 14195 Berlin, Germany

(Dated: September 3, 2021)

S1. METHODOLOGY

A. Density-functional theory calculations

All calculations are performed using the density-functional theory (DFT) as implemented in the Vienna *Ab initio* Simulation Package (VASP) code [1–3]. The electron-ion interactions are treated using the projector-augmented wave (PAW) [4, 5] method with a planewave kinetic energy cutoff of 500 eV. The generalized-gradient approximation due to Perdew, Burke and Ernzerhof (PBE) [6] is used to treat the exchange-correlation energy, augmented with the Grimme's D2 van der Waals (vdW) correction (PBE + D2) scheme [7] to calculate

---

[*] Contributed equally to this work

[†] aloysius.soon@yonsei.ac.kr

[‡] jin890@yonsei.ac.kr

all structural optimizations and surface energies. As reported Refs. 8 and 9 and references therein, the PBE+D2 approach used in this work describes the group 5 tetradymites well in terms of lattice constants, and provides a nice agreement to the experimental results. All atomic geometries and unit cell structures are fully optimized until changes in the total energy and forces are less than 10^{-5} eV and 10^{-4} eV/Å, respectively. Spin-orbit coupling (SOC) effects are neglected since it does not affect the order of surface energies considered in this work [10].

In addition, to evaluate the contribution of a solution-based environment to the surface stability of the M_2X_3, we utilized an implicit solvation model with a relative permittivity (ϵ) to account for solvation effects implemented in the VASP code (VASPsol) [11]. In order to mimic experimental synthesis conditions of M_2X_3 (i.e., solvothermal method [12–17]), we set three dielectric constants of 4, 40 and 80, to represent *low*, *moderate*, and *high* ϵ condition, respectively (e.g. polyvinyl pyrollidone ($\epsilon = 4$), ethylene glycol ($\epsilon = 37$), diethylene glycol ($\epsilon = 31.69$), and water ($\epsilon = 80$)). Within the solvation model, solvation energy of the surface (E_{sol}) is defined as:

$$E_{\text{sol}} = \frac{1}{2A}[E_{\text{sol}}^{\text{slab}} - E_{\text{vac}}^{\text{slab}}] \quad , \tag{S1}$$

where $E_{\text{sol}}^{\text{slab}}$, $E_{\text{vac}}^{\text{slab}}$, and A denotes the total energy of the slab in the solvent, in the vacuum, and the surface area, respectively.

For the slab calculations, 25 atomic layers (ALs) of (001) and 13 ALs of (015) and (110) surface slabs are modeled while preserving the inversion symmetry, and the innermost 5 ALs for (001) and 3 ALs for (015) and (110) surfaces are fixed in their bulk positions. In order to take surface defects into account, we have included four different types of surface point defects, such as cation vacancy (V_M), anion vacancy (V_X), cation antisite (M_X), and anion antisite (X_M). By combining different surface indicies and surface defects together, 40 different surface phases for all three tetradymite M_2X_3 (i.e., Bi_2Se_3, Bi_2Te_3, and Sb_2Te_3), total 120 surface phases were constructed (see Tabs. S3–S5). Considering possible diversity at the non-stoichiometric conditions, $p(2 \times 2)$ supercell is calculated exceptionally for (001) slab model (containing 100 atoms) while $p(1 \times 1)$ surface unit cell is used for (015) and (110) surfaces (containng 65 atoms). To avoid the spurious interactions between periodically repeated images, the vacuum region of at least 15 Å is introduced along the out-of-plane direction. The Brillouin zone integration is sampled with **k**-point grids of 12 × 12 × 1,

$4 \times 4 \times 1$, and $6 \times 3 \times 1$ for the (001), (015), and (110) $p(1 \times 1)$ surfaces, respectively. For the larger surface unit cells, the grids have been folded accordingly to obtain the same sampling of reciprocal space.

B. *Ab-initio* atomistic thermodynamics

The surface free energy (γ) of three surface models (i.e. (001), (015) and (110) surfaces) considered in this work is calculated under the *ab-initio* atomistic thermodynamics framework [12, 18–21], with the following definition:

$$\gamma(\mu_M, \mu_X) = \frac{1}{2A} \left(E^{\text{slab}} - N_M \mu_M - N_X \mu_X \right) \quad , \tag{S2}$$

where A, E^{slab}, and N_X (N_M) denoting the the surface area of the slab, DFT-calculated total energy of the slab, and the number of X (M) atoms, respectively. μ_X (μ_M) is the chemical potential of the X (M) species, which is derived from the relationship of $2\mu_X + 3\mu_M = E_{\text{f}}(M_2X_3)$ where $E_{\text{f}}(M_2X_3)$ is the formation energy of bulk M_2X_3. Having the condition of chemical potentials (i.e., $2\mu_X + 3\mu_M = E_{\text{f}}(M_2X_3)$), upper and lower limits of chemical potential can be understood as the chemical reservoir of respective species (i.e., bulk X phase and bulk M phase). For instance, assuming that Bi_2Se_3 nanoparticles are synthesized by mixing bulk Bi and bulk Se phases, upper (lower) limit of μ_{Bi} is the chemical potential of bulk Bi (bulk Se), which is understood as a Bi-rich (Se-rich) condition. In other words, going beyond these chemical potential limits implies the non-equilibrium condition with respect to bulk Bi and bulk Se.

Consequently, given that the condition of chemical potentials (i.e., $2\mu_X + 3\mu_M = E_f(M_2X_3)$) holds true, the Eq. S1 can be expressed as a function of μ_X,

$$\gamma(\mu_X) = \frac{1}{2A} \left[G^{\text{slab}} - \frac{N_M}{2} G^{\text{bulk}}_{M_2X_3} - \left(N_X - \frac{3}{2} N_M \right) \mu_X \right] \quad . \tag{S3}$$

This definition thus allows us to include various non-stoichiometric surfaces of M_2X_3 whose thermodynamic stability will be governed by the chemical potential change of the X species.

C. Gibbs–Wulff theorem

Having calculated surface free energies of different orientations via Eq. S3, we can predict crystal shapes according to the Gibbs-Wulff theorem [12, 20, 22–24]. The Gibbs–Wulff theorem provides a simple mathematical approach that predicts the shape of crystals or nanoparticles, whereby the total free energy of the crystal is minimum at a constant volume. The mathematical expression of Gibbs–Wulff theorem is given by:

$$r(d) = \min_{hkl} \left[\alpha \cdot \gamma \left(\mu_i \right) \right] \quad , \tag{S4}$$

where $r(d)$ represents the radius of the crystal shape in the direction of the vector, d and α is the proportionality constant. The directional vector, d, defines the normal vector to a particular crystal surface (hkl). $\gamma \left(\mu_i \right)$ is the surface energy value as a function of the chemical potential of the component i. For given condition (i.e. under specific μ_i), by minimizing the total surface free energy of the crystal at a constant volume and particular surface orientation, we can obtain the corresponding crystal morphology.

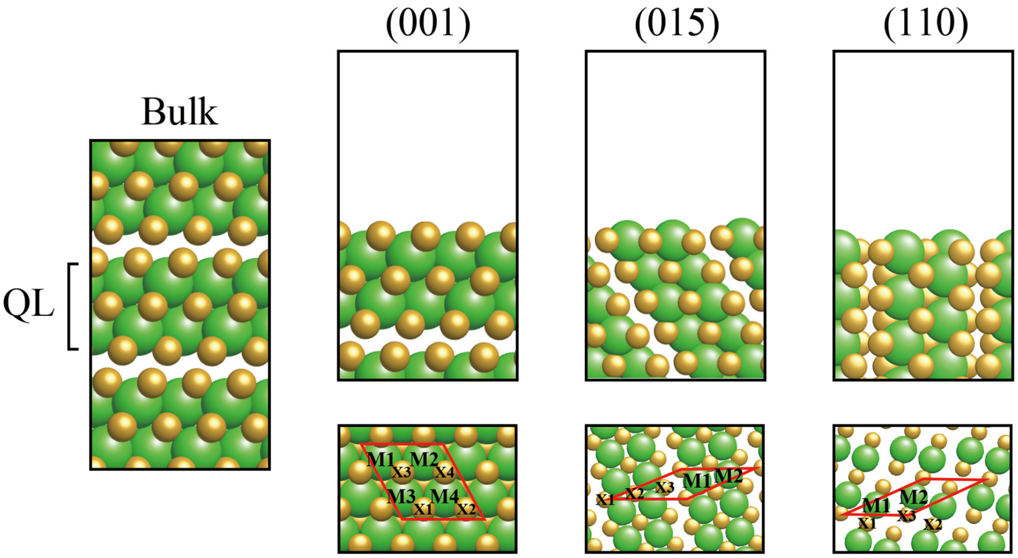

FIGURE S1. Top- and side- view of a unit cell of bulk M_2X_3 (M = Bi and Sb, X = Se and Te) and (001), (015), and (110) surface is shown. The five atomic layers ($X - M - X - M - X$) consist one quintuple layer (QL) and three QLs compose one unit cell of the bulk M_2X_3. Distinct atomic sites on the uppermost atomic layer of surface structures are labeled as well. Large green spheres and small gold spheres denotes the M and X atoms, respectively. Red boxes are used to indicate the unit cell.

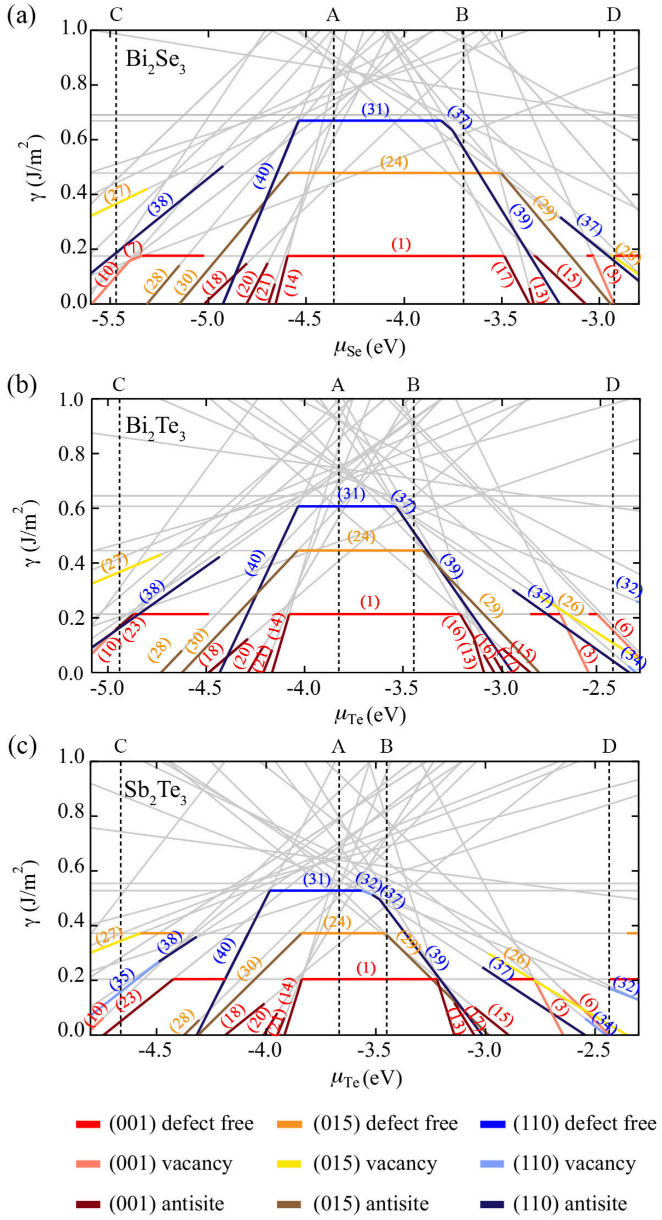

Figure S2. Calculated surface free energy (γ, in J$\cdot$m^{-2}) as a function of the anion chemical potential (μ_X, in eV) for (a) Bi$_2$Se$_3$, (b) Bi$_2$Te$_3$, and (c) Sb$_2$Te$_3$, under the vacuum condition. The surface free energies of the most favorable surface phases of (001), (015), and (110) are indicated by red-, orange-, and blue-colored lines, respectively. All other less stable surfaces are illustrated in gray lines. The thermodynamic equilibrium and non-equilibrium regions are separated by the vertical dotted lines labeled in A and B, which correspond to the reference bulk state of M and X, respectively (see Tab. S2 in Supplementary Materials for details). The number written above each line corresponds to the specific surface structure listed in the Tabs. S3-S5.

Side	Top	μ_{Se} (eV)	$d_{lat.}/d_{vert.}$
		-5.473	1.81
		-5.375	1.46
		-5.250	0.33
		-5.125	0.12
		-5.000	7.43
		-4.875	0.90
	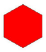	-4.750	3.91
	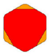	-4.625	4.57
	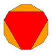	-4.500 ~ -3.875	2.71
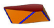	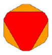	-3.750	2.71
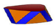	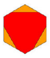	-3.698	2.71
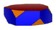		-3.625	2.71
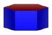	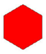	-3.500	1.93
		-3.375	8.47
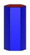		-3.250	0.42
		-3.125	4.41
		-3.000	0.39
		-2.926	0.87

FIGURE S3. The (meta-)stable crystal shapes, corresponding Se chemical potential, and measured aspected ratio of Bi_2Se_3 calculated in every 0.125 eV of μ_X specifically under the vacuum condition. The red-, orange- and blue-colored facets symbolize (001), (015) and (110), respectively.

Side	Top	μ_{Te} (eV)	$d_{\mathrm{lat.}}/d_{\mathrm{vert.}}$
		-4.942	0.96
		-4.875	0.93
		-4.750	1.23
		-4.625	0.01
		-4.500	0.45
		-4.375	1.24
	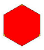	-4.250	5.77
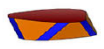	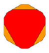	-4.125	3.70
		-4.000 ~ -3.625	2.09
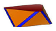		-3.500	2.09
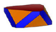		-3.451	2.09
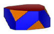	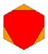	-3.375	2.00
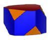		-3.250	1.46
		-3.125	2.44
		-3.000	14.81
		-2.875	3.99
		-2.750	0.95
		-2.625	1.45
		-2.500	0.38
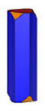		-2.437	0.28

Figure S4. The (meta-)stable crystal shapes, corresponding Se chemical potential, and measured aspected ratio of $\mathrm{Bi_2Te_3}$ calculated in every 0.125 eV of μ_X specifically under the vacuum condition. The red-, orange- and blue-colored facets symbolize (001), (015) and (110), respectively.

Side	Top	μ_{Te} (eV)	$d_{\mathrm{lat.}}/d_{\mathrm{vert.}}$
		-4.663	3.09
		-4.625	2.41
	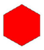	-4.500	1.68
		-4.375	0.01
		-4.250	0.24
		-4.125	3.54
		-4.000	13.23
	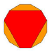	-3.875	3.17
		-3.750 ~ -3.500	1.81
		-3.451	1.78
		-3.375	1.50
		-3.250	1.02
		-3.125	1.16
		-3.000	0.20
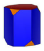		-2.875	0.85
		-2.750	0.69
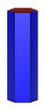		-2.625	0.29
		-2.500	0.61
		-2.437	8.24

FIGURE S5. The (meta-)stable crystal shapes, corresponding Se chemical potential, and measured aspected ratio of $\mathrm{Sb_2Te_3}$ calculated in every 0.125 eV of μ_X specifically under the vacuum condition. The red-, orange- and blue-colored facets symbolize (001), (015) and (110), respectively.

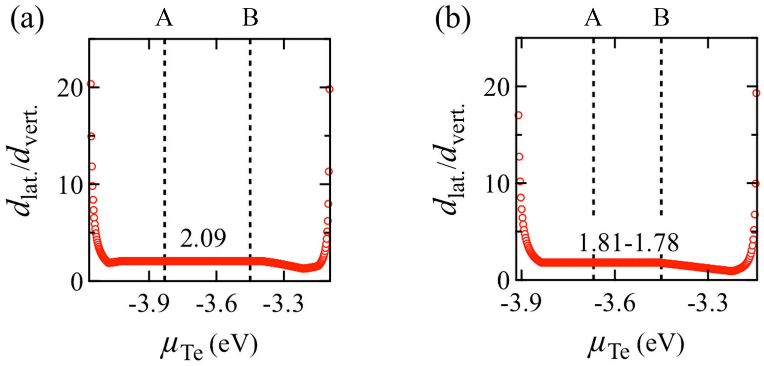

FIGURE S6. Measured aspect ratio of predicted crystal shapes, with respect to the μ_X for (a) Bi_2Te_3 ($-4.17 \leq \mu_{\mathrm{Te}} \leq -3.09$) and (b) Sb_2Te_3 ($-3.92 \leq \mu_{\mathrm{Te}} \leq -3.14$).

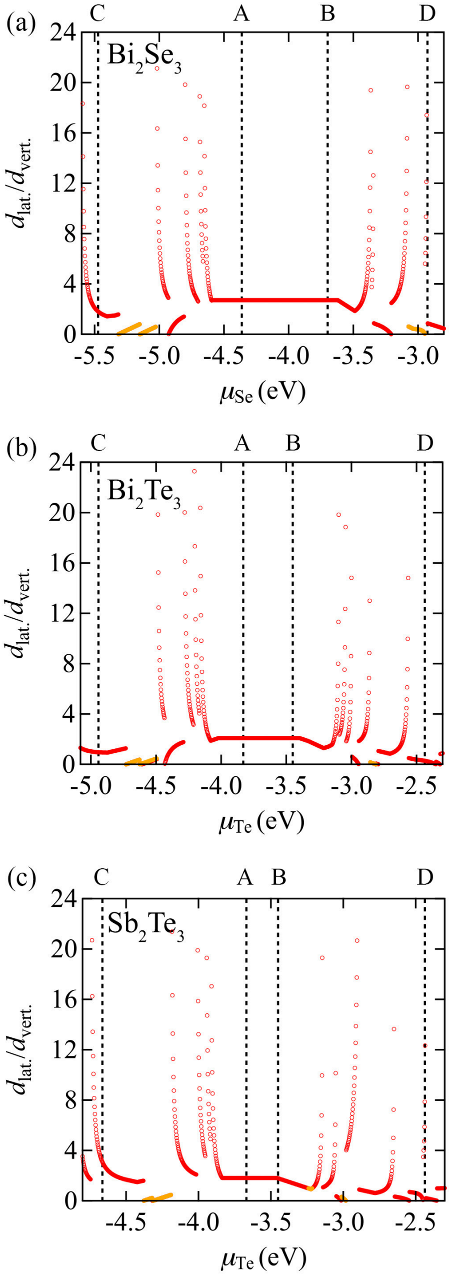

FIGURE S7. Measured aspect ratio of predicted crystal shapes, with respect to the μ_X for (a) Bi$_2$Se$_3$, (b) Bi$_2$Te$_3$, and (c) Sb$_2$Te$_3$ under vacuum condition. The yellow colored points represent the particular points where the highly isotropic particle with skewed cubic-like shape on it.

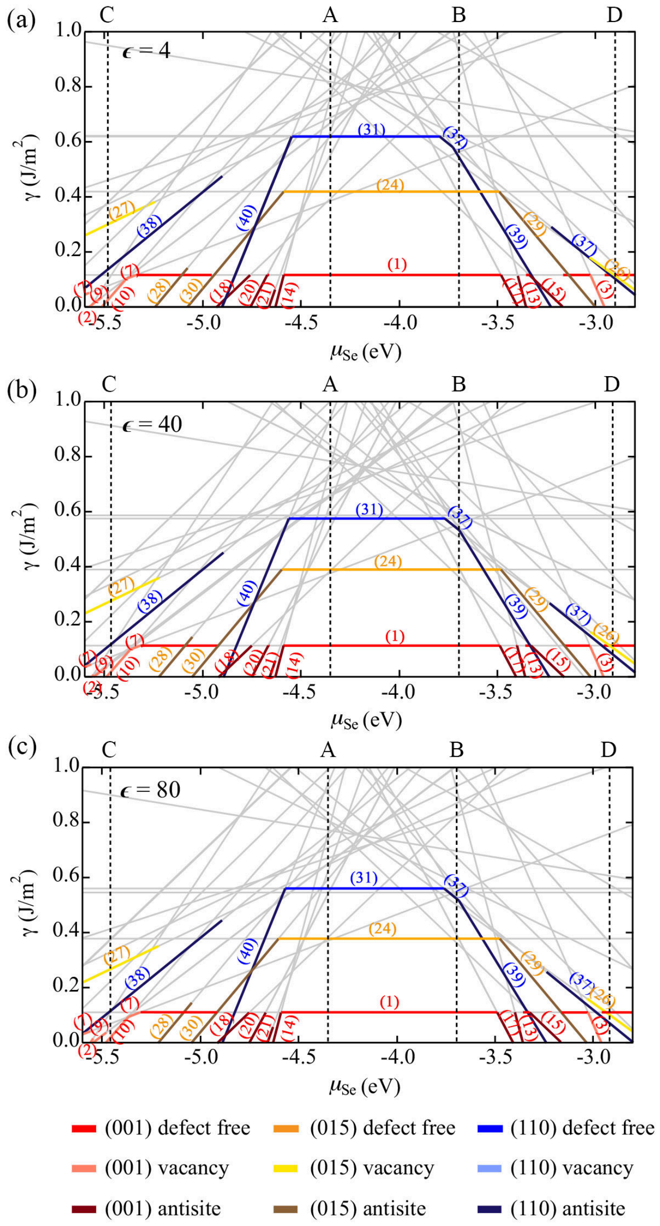

FIGURE S8. Calculated γ with respect to μ_X for Bi_2Se_3 under different dielectric mediums, (a) $\epsilon = 4$ (b) $\epsilon = 40$, and (c) $\epsilon = 80$. The surface free energies of the most favorable surface phases of (001), (015), and (110) are indicated by red-, orange-, and blue-colored lines, respectively. All other less stable surfaces are illustrated in gray lines. The thermodynamic equilibrium and non-equilibrium regions are separated by the vertical dotted lines labeled in A and B, which correspond to the reference bulk state of M and X, respectively (see Tab. S2 in Supplementary Materials for details). The number written above each line corresponds to the specific surface structure listed in the Tabs. S3-S5.

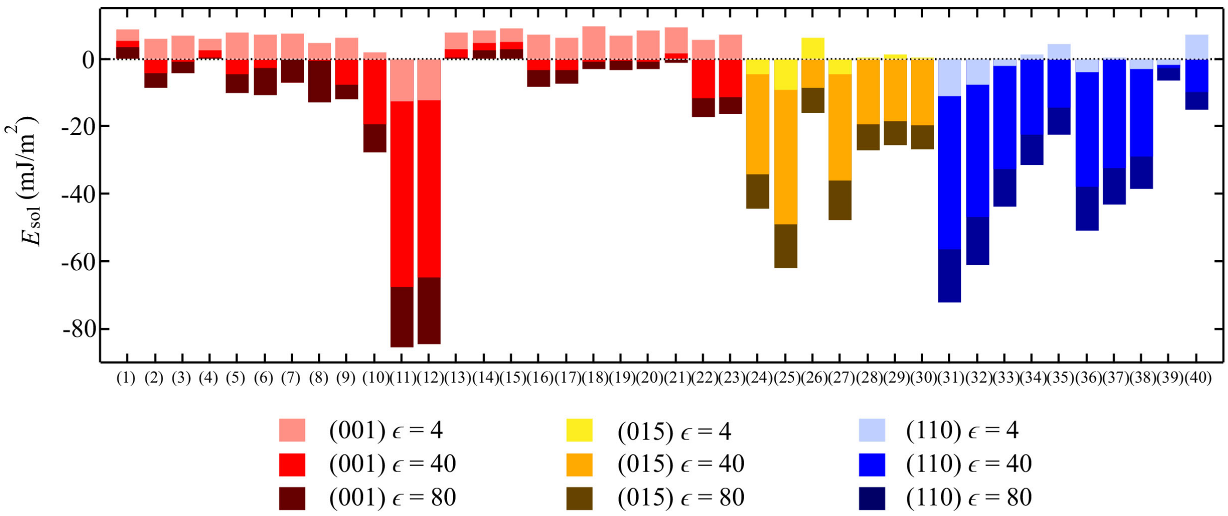

FIGURE S9. Calculated solvation energy (E_{sol}, in mJ/m^2) of all $\mathrm{Bi_2Se_3}$ surface structures discussed in this work. Detailed information of corresponding surface structures can be found in Tabs. S3−S5.

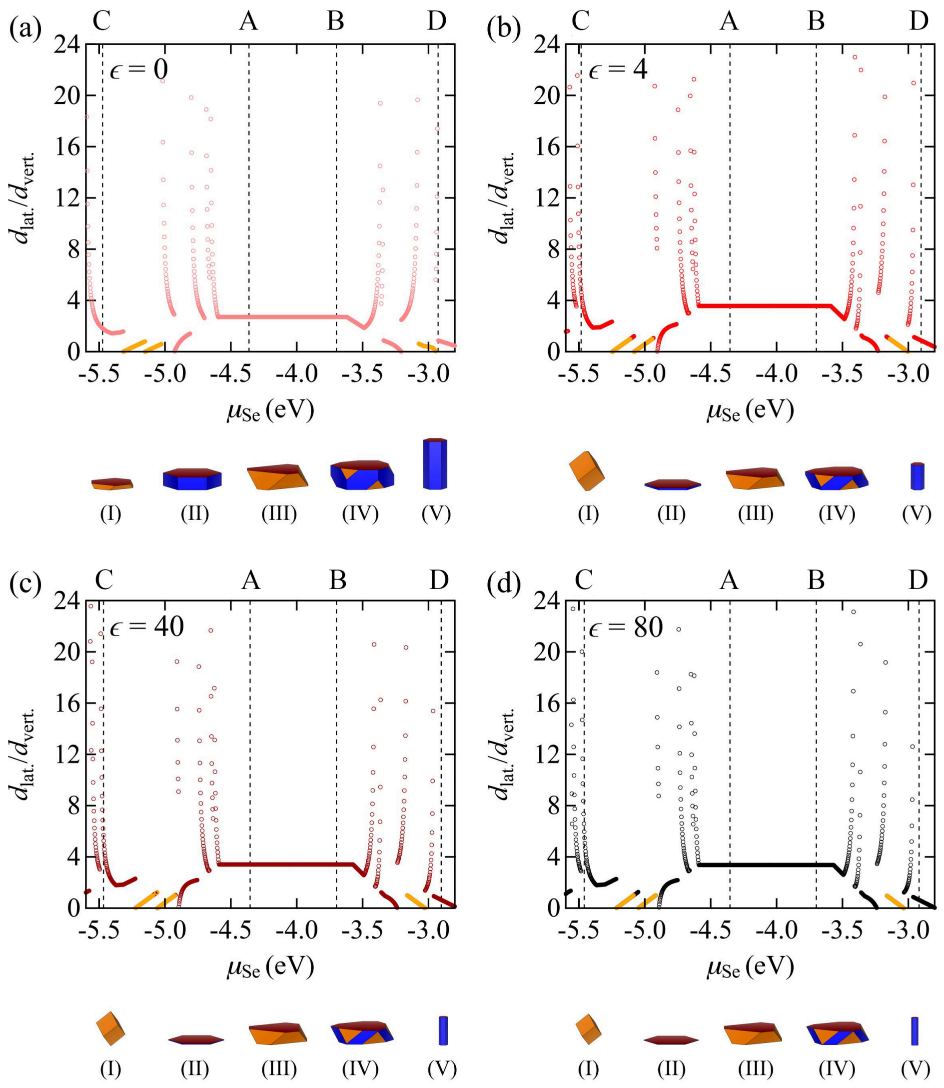

FIGURE S10. Measured aspect ratio of predicted crystal shapes, with respect to the μ_X for $\mathrm{Bi_2Se_3}$ under different dielectric mediums, (a) $\epsilon = 0$, (b) $\epsilon = 4$, (c) $\epsilon = 40$, and (d) $\epsilon = 80$. The thermodynamic equilibrium and non-equilibrium regions are separated by the vertical dotted lines labeled in A and B, which correspond to the reference bulk state of M and X, respectively (see Tab. S2 in Supplementary Materials for details). The representative crystal shapes for more intuitive comparisons, specifically under (I) = −5.00, (II) = −4.75, (III) = −4.50, (IV) = −3.625, and (V) = −3.25 eV of μ_X are plotted below.

Side	Top	μ_{Se} (eV)	$d_{\mathrm{lat.}}/d_{\mathrm{vert.}}$
		-5.483	4.75
		-5.375	1.89
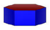		-5.250	2.34
		-5.125	0.89
		-5.000	0.58
		-4.875	1.30
		-4.750	24.25
	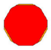	-4.625	15.57
	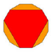	-4.500 ~ -3.698	3.57
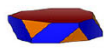		-3.625	3.57
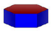	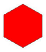	-3.500	2.69
		-3.375	3.58
		-3.250	0.46
		-3.125	0.88
		-3.000	2.22
		-2.903	0.88

FIGURE S11. The (meta-)stable crystal shapes, corresponding Se chemical potential, and measured aspected ratio of $\mathrm{Bi_2Se_3}$ calculated in every 0.125 eV of μ_X specifically under the $\epsilon = 4$ condition. The red-, orange- and blue-colored facets symbolize (001), (015) and (110), respectively.

Side	Top	μ_{Se} (eV)	$d_{\mathrm{lat.}}/d_{\mathrm{vert.}}$
		-5.466	5.48
		-5.375	1.81
		-5.250	2.17
		-5.125	0.74
		-5.000	0.43
		-4.875	1.20
		-4.750	63.94
		-4.625	17.16
		-4.500 ~ -3.698	3.41
		-3.625	2.67
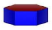		-3.500	2.67
		-3.375	3.75
		-3.250	0.27
		-3.125	0.74
		-3.000	2.03
		-2.903	0.64

FIGURE S12. The (meta-)stable crystal shapes, corresponding Se chemical potential, and measured aspected ratio of $\mathrm{Bi}_2\mathrm{Se}_3$ calculated in every 0.125 eV of μ_X specifically under the $\epsilon = 40$ condition. The red-, orange- and blue-colored facets symbolize (001), (015) and (110), respectively.

Side	Top	μ_{Se} (eV)	$d_{lat.}/d_{vert.}$
		-5.460	5.96
		-5.375	1.87
		-5.250	2.11
		-5.125	0.69
		-5.000	0.37
		-4.875	1.10
		-4.750	134.74
	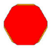	-4.625	18.14
	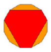	-4.500 ~ -3.698	3.36
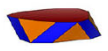	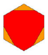	-3.625	3.36
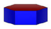		-3.500	2.67
		-3.375	3.85
		-3.250	0.21
		-3.125	0.68
		-3.000	1.96
		-2.919	0.64

FIGURE S13. The (meta-)stable crystal shapes, corresponding Se chemical potential, and measured aspected ratio of Bi_2Se_3 calculated in every 0.125 eV of μ_X specifically under the $\epsilon = 80$ condition. The red-, orange- and blue-colored facets symbolize (001), (015) and (110), respectively.

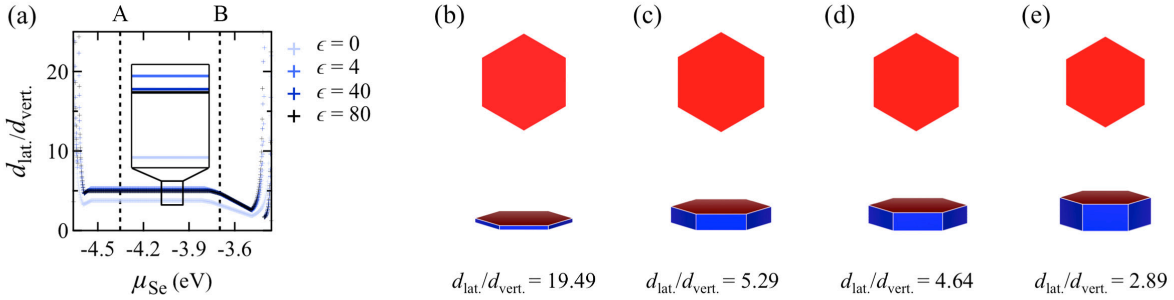

FIGURE S14. (a) Measured aspect ratio of predicted crystal shapes for Bi_2Se_3, with respect to the μ_{Se}. Different dielectric environments are represented by different colors of cross symbols. (b-e) Predicted crystal shapes and corresponding aspect ratio of Bi_2Se_3 at -4.625, -4.362, -3.698, and -3.520 eV, under $\epsilon = 4$ condition. Red and blue colored region denotes (001) and (110) surface, respectively.

Table S1. Calculated surface energies (γ, in J/m^2) of three stoichiometric surfaces (i.e. (001), (015) and (110)) of M_2X_3 (M = Bi and Sb, X = Se and Te) under the vacuum condition ($\epsilon = 0$), and γ of three stoichiometric surfaces of Bi$_2$Se$_3$ under different dielectric conditions (i.e. ϵ =4, 40, and 80).

Materials	$\gamma_{(001)}$	$\gamma_{(015)}$	$\gamma_{(110)}$
Bi$_2$Se$_3$ ($\epsilon = 0$)	0.18	0.48	0.67
Bi$_2$Te$_3$ ($\epsilon = 0$)	0.21	0.45	0.61
Sb$_2$Te$_3$ ($\epsilon = 0$)	0.21	0.37	0.53
Bi$_2$Se$_3$ ($\epsilon = 4$)	0.12	0.42	0.62
Bi$_2$Se$_3$ ($\epsilon = 40$)	0.11	0.39	0.58
Bi$_2$Se$_3$ ($\epsilon = 80$)	0.11	0.38	0.56

Table S2. Chemical potential of X corresponding to the equilibrium (A and B) and metastable (C and D) boundary of M_2X_3 under the vacuum condition ($\epsilon = 0$), and Bi$_2$Se$_3$ under different dielectric conditions (i.e. ϵ =4, 40, and 80).

Materials	C	A	B	D
Bi$_2$Se$_3$ ($\epsilon = 0$)	−5.473	−4.362	−3.698	−2.926
Bi$_2$Te$_3$ ($\epsilon = 0$)	−4.942	−3.831	−3.451	−2.437
Sb$_2$Te$_3$ ($\epsilon = 0$)	−4.663	−3.669	−3.451	−2.437
Bi$_2$Se$_3$ ($\epsilon = 4$)	−5.483	−4.354	−3.698	−2.903
Bi$_2$Se$_3$ ($\epsilon = 40$)	−5.466	−4.354	−3.698	−2.903
Bi$_2$Se$_3$ ($\epsilon = 80$)	−5.460	−4.354	−3.698	−2.919

Table S3. Numerical labeling of M_2X_3 structures for 23 different (non-)stoichiometric (001) surfaces. Four distinct atomic point defects (i.e. V_M, V_X, M_X, and X_M) and their possible combinations are included. Here, the V_M, V_X, M_X, and X_M corresponds to the cation vacancy, anion vacancy, anion antisite and cation antisite defects.

Structure number	M_2X_3 (001)
(1)	Defect free
(2)	V_{X1}
(3)	V_{M1}
(4)	(2x2) V_{M1}
(5)	(2x2) $V_{M1} + V_{M2}$
(6)	(2x2) $V_{M1} + V_{M4}$
(7)	(2x2) V_{X4}
(8)	(2x2) $V_{X3} + V_{X4}$
(9)	(2x2) $V_{X1} + V_{X4}$
(10)	(2x2) $V_{X2} + V_{X3} + V_{X4}$
(11)	(2x2) $V_{M1} + V_{M2} + V_{X1} + V_{X3}$
(12)	(2x2) $V_{M1} + V_{M4} + V_{X2} + V_{X3} + V_{X4}$
(13)	X_{M1}
(14)	M_{X1}
(15)	(2x2) X_{M1}
(16)	(2x2) $X_{M1} + X_{M2}$
(17)	(2x2) $X_{M1} + X_{M4}$
(18)	(2x2) M_{X4}
(19)	(2x2) $M_{X3} + M_{X4}$
(20)	(2x2) $M_{X1} + M_{X4}$
(21)	(2x2) $M_{X2} + M_{X3} + M_{X4}$
(22)	(2x2) $M_{X1} + M_{X3} + M_{X4} + X_{M1} + X_{M2}$
(23)	(2x2) $M_{X2} + M_{X3} + M_{X4} + X_{M1} + X_{M4}$

Table S4. Numerical labeling of M_2X_3 structures for 7 different (non-)stoichiometric (015) surfaces.

Structure number	M_2X_3 (015)
(24)	Defect free
(25)	V_{X2}
(26)	V_{M1}
(27)	V_{X1}
(28)	M_{X2}
(29)	X_{M1}
(30)	M_{X1}

Table S5. Numerical labeling of M_2X_3 structures for 10 different (non-)stoichiometric (110) surfaces.

Structure number	M_2X_3 (110)
(31)	Defect free
(32)	V_{M2}
(33)	V_{X3}
(34)	$V_{M1} + V_{M2}$
(35)	$V_{X1} + V_{X2} + V_{X3}$
(36)	$V_{M2} + V_{X3}$
(37)	X_{M2}
(38)	M_{X3}
(39)	$X_{M1} + X_{M2}$
(40)	$M_{X1} + M_{X2} + M_{X3}$

---

[1] G. Kresse, J. Hafner. Ab Initio Molecular Dynamics for Liquid Metals. *Phys. Rev. B* **1993**, *47*, 558.

[2] G. Kresse, J. Hafner. Ab Initio Molecular-Dynamics Simulation of the Liquid-Metal-Amorphous-Semiconductor Transition in Germanium. *Phys. Rev. B* **1994**, *49*, 14251.

[3] G. Kresse, J. Furthmüller. Efficient Iterative Schemes for Ab Initio Total-Energy Calculations Using a Plane-Wave Basis Set. *Phys. Rev. B* **1996**, *54*, 11169.

[4] G. Kresse, D. Joubert. From Ultrasoft Pseudopotentials to the Projector Augmented-Wave Method. *Phys. Rev. B* **1999**, *59*, 1758.

[5] P. E. Blöchl. Projector Augmented-Wave Method. *Phys. Rev. B* **1994**, *50*, 17953.

[6] J. P. Perdew, K. Burke, M. Ernzerhof. Generalized Gradient Approximation Made Simple. *Phys. Rev. Lett.* **1996**, *77*, 3865.

[7] S. Grimme. Semiempirical GGA-Type Density-Functional Constructed with a Long-Range Dispersion Correction. *J. Comput. Chem.* **2006**, *27*, 1787–1799.

[8] C. Li, T. Winzer, A. Walsh, B. Yan, C. Stampfl, A. Soon. Stacking-Dependent Energetics and Electronic Structure of Ultrathin Polymorphic V_2VI_3 Topological Insulator Nanofilms. *Phys. Rev. B* **2014**, *90*, 075438.

[9] W. Jang, J. Lee, C. In, H. Choi, A. Soon. Designing Two-Dimensional Dirac Heterointerfaces of Few-Layer Graphene and Tetradymite-Type Sb_2Te_3 for Thermoelectric Applications. *ACS Appl. Mater. Interfaces* **2017**, *9*, 42050–42057.

[10] N. Wang, Y. Sun, Y. Zhang, D. West, W. Duan, S. Zhang. Stability Investigations on the Non-vdW-Exfoliated Surfaces of the Topological Insulator Bi_2Te_3: A First-Principles Study. *Phys. Rev. B* **2016**, *93*, 115306.

[11] K. Mathew, R. Sundararaman, K. Letchworh-Weaver, T. A. Arias, R. G. Hennig. Implicit Solvation Model for Density-Fuctional Study of Nanocrystal Surfaces and Reaction pathways. *J. Chem. Phys.* **2014**, *140*, 084106.

[12] G. Park, J. Lee, S. Moon, H. Yang, A. Giri, J. Kwak, Y.-K. Jung, A. Soon, U. Jeong. Eventual Chemical Transformation of Metals and Chalcogens into Metal Chalcogenide Nanoplates through a Surface Nucleation-Detachment-Reorganization Mechanism. *Chem. Mater.* **2017**, *29*, 3219–3227.

[13] J. Song, F. Xia, M. Zhao, Y. L. Zhong, W. Li, K. P. Loh, R. A. Caruso, Q. Bao. Solvothermal Growth of Bismuth Chalcogenide Nanoplatelets by the Oriented Attachment Mechanism: An *in Situ* PXRD Study. *Chem. Mater.* **2015**, *27*, 3471–3482.

[14] X. He, H. Zhang, W. L. and. PVP-Assisted Solvothermal Synthesis of High-Yielded Bi_2Te_3 Hexagonal Nanoplates: Application in Passively Q-Switched Fiber Laser. *Sci. Rep.* **2015**, *5*, 15868.

[15] M. Takashiri, S. Kai, K. Wada, S. Tskasugi, K. Tomita. Role of Stirring Assist During Solvothermal Synthesis for Preparing Single-crystal Bismuth Telluride Hexagonal Nanoplates. *Mater. Chem. Phys.* **2016**, *173*, 213.

[16] K. Wada, K. Tomita, M. Takashiri. Fabrication of Bismuth Telluride Nanoplates via Solvothermal Synthesis Using Different Alkalis and Nanoplate Thin Films by Printing Method. *J. Cryst. Growth* **2017**, *468*, 194–198.

[17] X. Zhang, H. Cheng, H. Zhang. Recent Progress in the Preparation, Assembly, Transformation, and Applications of Layer-Structured Nanodisks beyond Graphene. *Adv. Mater.* **2017**, *29*, 1701704.

[18] A. Soon, M. Todorova, B. Delly, C. Stampfl. Thermodynamic Stability and Structure of Copper Oxide Surfaces: A First-Principles Investigation. *Phys. Rev. B* **2007**, *75*, 125420.

[19] Y. Kwon, A. Soon, H. Han, H. Lee. Shape Effects of Cuprous Oxide Particles on Stability in Water and Photocatalytic Water Splitting. *J. Mater. Chem. A* **2015**, *3*, 156.

[20] T. Lee, B. Delley, C. Stampfl, A. Soon. Environment-Dependent Nanomorphology of TiN: The Influence of Surface Vacancies. *Nanoscale* **2012**, *4*, 5183.

[21] J. Kwak, C.-E. Kim, Y. Min, J.-H. Lee, A. Soon. The Effect of Se Doping on the Growth of Te Nanorods. *Cryst. Eng. Comm.* **2015**, *17*, 5734.

[22] G. Wulff. Zur Frage der Geschwindigkeit des Wachstums und der Auflösung der Krystallflächen. *Z. Kristallogr.* **1901**, *34*, 449–530.

[23] T. Lee, Y. Lee, W. Jang, A. Soon. Understanding the Advantage of Hexagonal WO_3 as an Efficient Photoanode for Solar Water Splitting: A First-Principles Perspective. *J. Mater. Chem. A* **2016**, *4*, 11498.

[24] S.-H. Yoo, J.-H. Lee, B. Delly, A. Soon. Why Does Bromine Square Palladium Off? An Ab Initio Study of Brominated Palladium and Its Nanomorphology. *Phys. Chem. Chem. Phys.* **2014**, *16*, 18570–18577.